applied sciences

MDPI

Article

Investigation of the Thermodynamics for the Removal of As(III) and As(V) from Water Using Synthesized ZnO Nanoparticles and the Effects of pH, Temperature, and Time

Helia Magali Morales [1,2], Grecia Torreblanca [1], Arnulfo Mar [1], Mataz Alcoutlabi [3], Thomas Mark Eubanks [1], Erik Plata [1] and Jason George Parsons [4,*]

[1] Department of Chemistry, University of Texas Rio Grande Valley, 1 West University Blvd., Brownsville, TX 78521, USA; helia.morales@utrgv.edu (H.M.M.); grecia.torreblanca01@utrgv.edu (G.T.); erik.plata@utrgv.edu (E.P.)
[2] Escuela de Ingenieria y Ciencias, Tecnologico de Monterrey, Av E Garza Sada # 2501, Monterrey 64849, Mexico
[3] Department of Mechanical Engineering, University of Texas Rio Grande Valley, 1 West University Blvd., Brownsville, TX 78521, USA
[4] School of Earth Environmental, and Marine Science, University of Texas Rio Grande Valley, 1 West University Blvd., Brownsville, TX 78521, USA
* Correspondence: jason.parsons@utrgv.edu

Abstract: In the present study, the removal of both As(III) and As(V) from aqueous solutions using synthesized ZnO nanomaterials was achieved. The ZnO nanomaterial was synthesized using a precipitation technique and characterized using XRD, SEM, and Raman spectroscopy. XRD confirmed the ZnO nanoparticles were present in the hexagonal wurtzite structure. SEM of the particles showed they were aggregates of triangular and spherical particles. The average nanoparticle size was determined to be 62.03 ± 4.06 nm using Scherrer's analysis of the three largest diffraction peaks. Raman spectroscopy of the ZnO nanoparticles showed only ZnO peaks, whereas the after-reaction samples indicated that As(V) was present in both As(V)- and As(III)-reacted samples. The adsorption of the ions was determined to be pH-independent, and a binding pH of 4 was selected as the pH for reaction. Batch isotherm studies showed the highest binding capacities occurred at 4 °C with 5.83 mg/g and 14.68 mg/g for As(III) and As(V), respectively. Thermodynamic studies indicated an exothermic reaction occurred and the binding of both As(III) and As(VI) took place through chemisorption, which was determined by the ΔH values of −47.29 and −63.4 kJ/mol for As(V) and As(III), respectively. In addition, the change in Gibbs free energy, ΔG, for the reaction confirmed the exothermic nature of the reaction; the spontaneity of the reaction decreased with increasing temperature. Results from batch time dependency studies showed the reaction occurred within the first 60 min of contact time.

Keywords: nanoparticles; ZnO; As(III); As(V); chemisorption

check for updates

Citation: Morales, H.M.; Torreblanca, G.; Mar, A.; Alcoutlabi, M.; Eubanks, T.M.; Plata, E.; Parsons, J.G. Investigation of the Thermodynamics for the Removal of As(III) and As(V) from Water Using Synthesized ZnO Nanoparticles and the Effects of pH, Temperature, and Time. *Appl. Sci.* **2023**, *13*, 10525. https://doi.org/10.3390/app131810525

Academic Editor: Ramaraj Boopathy

Received: 30 August 2023
Revised: 13 September 2023
Accepted: 19 September 2023
Published: 21 September 2023

1. Introduction

Arsenic is an element of interest for both environmental and human health as it is a well-known toxin and carcinogen. The natural sources of arsenic include volcanic eruptions, mineral dissolution, and forest fires. Anthropogenic activities releasing arsenic into the environment include smelting/mining activities, burning of fossil fuels, and sulfuric acid production [1–6].

It is well known that inorganic and methylated As(III) compounds are typically more toxic than As(V) [7–9]. In addition, inorganic arsenic compounds are known to be more toxic than organic arsenic compounds [8–13]. After ingestion, soluble arsenic species can be absorbed, and as a result, As(III) can inhibit sulfhydryl-containing enzymes, which interrupt enzymatic activity [14]. As(V) is known to compete with phosphate,

thus inhibiting the formation of adenosine triphosphate and interfering with normal cell function [3,14]. Acute exposure to high doses of arsenic is known to cause health problems such as hyperkeratosis, cutaneous malignant tumors, alopecia, peripheral neuropathy, anemia, and skin cancer [1–3,14,15]. In order to reduce the risk of As exposure, numerous countries have adopted a 10 µg/L limit as their drinking water standard, while other countries have maximum As limits at 50 µg/L [2,7,16–19].

The removal of arsenic from aqueous solutions has been shown to be dependent on the oxidation state, concentration, pH, and ionic strength. Arsenic removal from water has been achieved using technologies such as membrane technology, adsorption, ion exchange, coagulation/flocculation, reverse osmosis, electrochemical, and bioremediation [20–29]. However, many of these technologies are ineffective or inefficient, and cost-prohibitive [30]. There has been increased interest in adsorption methods due to their cost and lack of by-products. Typically, adsorbents can be recycled, and process operation can be flexible [4,22].

Recently, the use of nanosorbents has become of interest due to their high surface area to volume ratio, the high number of active sites, and strong reactivity. The most studied nanoparticles to remove As from water include: metal oxides, metallic, bimetallic, zeolites, ferrite, polymers, activated alumina, and activated carbon [4,22,31]. Various metal oxides based nanosorbents for arsenic remediation have been prepared, which include Fe_2O_3, Fe_3O_4, Mn_3O_4, $MnFe_2O_4$, and ZnO [4,32–36]. As well, mixed metal oxide materials such as Fe-Ce, Fe-Mn, Fe-Ti, Ce-Ti, Fe-Zr, Fe-Cu, Mn-Co, and Fe-Cr have been synthesized and tested for As adsorption [4,32–36].

Singh et al. found that acetate-functionalized ZnO particles effectively removed arsenic from 2000 ppb to less than 10µg/L [37]. Kataria and Garg studied the adsorption of Cd(II), Pb(II), As(III), and Se(IV) using ZnO nanoflowers in multi-metal systems using an adsorption dose of 0.8 g/mL [38]. The removal efficiency was 57% for Cd(II) and 99% for Pb(II). Cu (II), As(III), and Se(IV) adsorption efficiencies were greater than 75% [38], whereas Gu et al. found that ZnO nanoparticles removed up to 88.57 mg/g of Cr(III) ions under optimal reaction conditions [39]. Cantu et al. investigated the binding of As(III) and As(V) to Fe_7S_8 and showed a pH-independent binding process and approximately 100% binding of both ions from pH 3 through pH 6 [40]. Parsons et al. developed Fe_3O_4, Mn_3O_4, and $FeMn_2O_4$ nanomaterials for the removal of As(III) and As(VI) from solution [30]. The Fe_3O_4, Fe_2MnO_4, and Mn_3O_4 showed binding capacities of 0.0323, 0.7182, and 0.0089 mg/g for As(III), respectively, whereas the binding of As(V) from aqueous solution showed capacities of 1.575, 2.125, and 0.212 mg/g for the Fe_3O_4, Fe_2MnO_4, and Mn_3O_4, respectively. Luther et al. investigated the binding of As(III) and As(V) to Fe_3O_4 and Fe_2O_3 nanomaterials, which showed pH-independent binding of both As(III) and As(V) from pH 6–10 [41]. In addition, the binding capacities after 1 h of contact showed binding capacities of 1.250 and 4.600 mg/g for As(III) and As(V) for Fe_2O_3. The Fe_3O_4 nanomaterial showed binding capacities of 8.196 and 6.711 mg/g for the binding of As(III) and As(V), respectively.

In the present study, ZnO was synthesized through a precipitation method. The synthesized ZnO nanoparticles were characterized using XRD, SEM and Raman spectroscopy to determine crystallinity, phase, and morphology. In addition, the samples were analyzed using XRD and Raman spectroscopy after reaction with the As(III) and As(V) ions to determine if any changes in the material phase or the presence of reaction products could be observed. Batch studies were performed to determine the effects of pH, temperature, time, and binding capacity on the As(III) and As(V) binding. The batch isotherm studies, and time dependency studies were performed to investigate the thermodynamic parameters of the binding and the time dependency of the binding process. ZnO was selected as the adsorbent to be investigated because of its properties, especially its cost-effective synthesis. The favorable synthesis properties did not require the need of surfactants, aqueous solution chemistry, and nor the need to calcine or convert the product at high temperatures. In fact, there is a potential for ZnO to be widely used for the removal of As(III) and As(V) from aqueous solution.

2. Methods

2.1. Materials

All chemicals were of analytical grade and used without further purification. NaOH, NaCl, KCl, $Zn(NO_3)_2 \cdot 6H_2O$, $MgCl_2 \cdot 6H_2O$, $NaNO_3$, Na_2SO_4, and Na_2HPO_4 were obtained from Fischer Scientific and As_2O_3, and $Na_2HAsO_4 \cdot 7H_2O$ were obtained from Alfa Aesar. The deionized water used in the studies had a resistance of 18 MΩ·cm and was generated by a Milli-Q water purification system (Millipore, Burlington, MA, USA). As(III) and As(V) solutions were prepared dissolving either As_2O_3 or $Na_2HAsO_4 \cdot 7H_2O$ in 18 MΩ·cm DI water, respectively.

2.2. Synthesis of ZnO Nanomaterials

The ZnO nanoparticles were synthesized by dissolving $Zn(NO_3)_2$ in 18 MΩ cm DI water and precipitated as the metal hydroxide using NaOH. In brief, 150 mL of 1 $molL^{-1}$ NaOH solution was added dropwise to 500 mL of 60 $mmolL^{-1}$ $Zn(NO_3)_2$ solution under continuous stirring. The resulting mixture was heated at 50 °C for 2 h resulting in a milky white solution. The solution was centrifuged at 3000 rpm for 5 min, and the ZnO nanoparticles were collected. The collected nanoparticles were washed three times with DI water, and once with acetone. The washing was performed by centrifuging the particles, followed by resuspension of the nanoparticle in clean solvent. Once the particles were separated from the solution, they were dried overnight in an oven at 75 °C.

2.3. Adsorbent Characterization

ZnO nanoparticle characterization was performed using powder X-Ray Diffraction (XRD). The ZnO nanomaterial was homogenized by grinding the sample into a fine powder in a mortar and pestle. The XRD data were collected using a Bruker D2 phaser diffractometer fitted with a cobalt source (Kα = 1.789Å) and an iron filter. The patterns were collected from 10 to 80° 2θ with a 0.05° step and a 1s counting time. The fitting of the crystal structure was performed using the Le Bail fitting procedure in the Fullprof Suite software (Version January-2021) and crystallographic data from the literature [42,43]. SEM data were collected using a Zeiss LEO LS 10 SEM microscope operating at 9 keV and a 2.5 A current with a working distance of 6.0 mm. The sample preparation for SEM characterization consisted of sputter coating the samples with a AuPd alloy for 30 s Zeta potential of the ZnO nanoparticles was measured by a Malvern Zetasizer Nano Series Nano ZS90 instrument at pH values between 2 and 6. The ZnO NPs were suspended in 18 MΩ water while the pH of the ZnO aqueous solution was adjusted to the desired pH value using either dilute HNO3 or NaOH. The NPs were then equilibrated in solution to mimic the reaction conditions. The Zeta potential measurements were taken using the DTS1070 disposable cells. The RAMAN spectra were recorded using a Rigaku FirstGaurd hand-held RAMAN spectrometer equipped with a 754 nm laser. The spectra collection consisted of 100 co-additions at a 1000 ms sampling time and recorded from 200 cm^{-1} to 1000 cm^{-1} and the laser power was set to 100 mW.

2.4. ICP-OES Analysis

The ICP-OES analysis of the samples was performed using a Perkin Elmer Optima 8300 ICP-OES (Shelton CT) with the Winlab32 software. The data collection parameters are shown in Table 1. All calibration curves obtained had correlation coefficients of (R^2) 0.99 or better.

Table 1. Operational parameters for ICP-OES.

Parameter	Setting
L	193.696 nm
RF power	1500 W
Nebulizer	Gemcone (low flow)
Plasma flow	15 L min^{-1}
Auxiliary flow	0.2 L min^{-1}
Nebulizer flow	0.55 L min^{-1}
Sample flow	1.50 L min^{-1}
Injector	2.0 mm Alumina
Spray chamber	Cyclonic
Integration time	20 s
Replicates	3

2.5. pH Studies

The binding of the As(III) and As(V) was performed over a pH range of 2 through 6 using either 300 ppb As(III) or As(V) solutions. The pH adjustment of the As stock solutions was performed using either dilute NaOH or dilute HCl solutions. The reaction samples were prepared by adding 4 mL of the pH-adjusted solutions of either As(III) or As(V) to 10 mg of ZnO nanoparticles into 5 mL polyethylene test tubes. Control samples consisted of only As(III) and As(V) solutions without ZnO nanoparticles. All reaction and control samples were tested in triplicate for statistical purposes. The reaction and control samples were equilibrated for one hour at room temperature on a nutating mixer at a constant speed of 24 rpm. After equilibration, the samples and controls were centrifuged at 3500 rpm for 5 min, and the supernatants were decanted and stored in clean test tubes for analysis using ICP-OES.

2.6. Adsorption Isotherms

Batch adsorption isotherm studies were performed at the optimum binding pH of pH 4. Stock solutions of either As(III) or As(V) were prepared at concentrations of 3, 30, 100, 300, and 1000 ppm, and pH adjusted to pH 4. The samples were prepared by adding 4 mL of either As(III) or As(V) solutions to 10 mg of ZnO nanoparticles in a 5 mL polyethylene test tube. Control samples consisting of only As(III) and As(V) solutions were also prepared and treated the same as the samples. Both the reaction and control samples were prepared in triplicate for statistical purposes. All samples were equilibrated on a nutating mixer at a speed of 24 rpm. The reactions were performed at temperatures of 4, 22, and 45 °C. After equilibration, the samples were centrifuged at 3500 rpm for 5 min, and the supernatants were decanted and stored for analysis using ICP-OES.

2.7. Time Dependency Studies

Batch studies were performed to determine time dependency of the binding of either As(III) or As(V) to the synthesized ZnO nanomaterial. Solutions of either 30 ppm of As(III) or 30 ppm As(V) were prepared at the optimum binding pH of 4.0. The samples were prepared by adding 4 mL of the pH-adjusted solutions of either As(III) or As(V) to 10 mg of ZnO in 5 mL polyethylene test tubes. Control samples consisted of only As(III) or As(V) ions in solution without the ZnO nanoparticles. The reaction and control samples were performed in triplicate for statistical purposes and were then equilibrated at time intervals of 15, 30, 60, and 90 min on a nutating mixer at a mixing speed of 24 rpm. Furthermore, the reactions were performed at temperatures of 4, 22, and 45 °C. After equilibration, the samples were centrifuged at 3500 rpm for 5 min, and the supernatants were decanted and stored in clean test tubes for analysis using ICP-OES.

3. Results and Discussion

3.1. X-ray Diffraction

Figure 1 shows the X-ray diffraction pattern collected for the ZnO nanoparticles prepared by the precipitation technique. The observed diffraction peaks located at 37, 40.05, 42, 51, 67.05, 74.97, and 79° were indexed to ZnO and correspond to the 100, 002, 101, 102 and 110 diffraction planes observed in the hexagonal wurtzite structure, respectively [42,44]. The diffraction pattern confirmed the synthesized nanomaterial was ZnO. The diffraction pattern was fitted using the Le Bail fitting procedure in the Fullprof software, and the fitting results are shown in Table 2. The fitting showed the ZnO had a hexagonal space group ($P6_3/mc$) with refined lattice parameters of a = 3.245 Å, b = 3.245 Å, c= 5.199 Å with cell angles of $\alpha = \beta = 90°$, and $\gamma = 120°$, which are in agreement with results reported on ZnO. In addition, the χ^2 value (indicator of goodness of fit) of the fitting was 3.08, which indicated a good agreement between the data and reported results on the ZnO crystal structure [42,44]. Further analysis of the diffraction data showed that the average crystalline size of the ZnO nanosorbent was calculated using Scherrer's equation, as shown below:

$$d = \frac{0.9\lambda}{BCos\frac{2\theta}{2}} \quad (1)$$

where d is the diameter or crystallite size, 0.9 is a correction factor for the Gaussian fitting, λ is the Co K_α = 1.789 Å, B is the Full-Width Half Maximum (FWHM) of the diffraction peak, $cos2\theta/2$ is the position of the diffraction peak. The average crystallite size was determined based on the most prominent diffraction peaks: the 100 (27.21 nm), 002 (30.0 nm), and 100 (23.9 nm) diffraction planes, which averaged to 62.0 ± 4.06 nm.

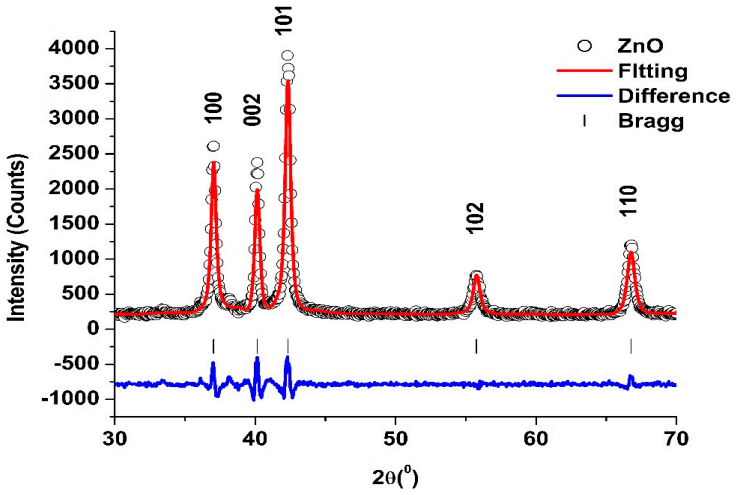

Figure 1. Powder XRD and Le Bail fitting of the synthesized ZnO nanomaterial.

Table 2. Le Bail fitting results of ZnO nanoparticle sample.

Sample	a (°A)	b (°A)	c (°A)	$\alpha°$	$\beta°$	$\gamma°$	χ^2
ZnO_{syn}	3.245(8)	3.245(8)	5.199(8)	90.0	90.0	120.0	3.08
ZnO_{lit}	3.2417	3.2417	5.1876	90.0	90.0	120.0	

The SEM of the synthesized ZnO nanoparticles is shown in Figure 2. The image showed that the nanoparticles were clustered and consisted of a mixture of triangular-shaped platelets and small spherical particles. The observed clustering of the particles, more than likely, was due to the lack of surfactants used in synthesis. The exclusion of surfactants aimed at generating the ZnO nanoparticles with a clean surface available for the binding of the As(III) and As(V) ions.

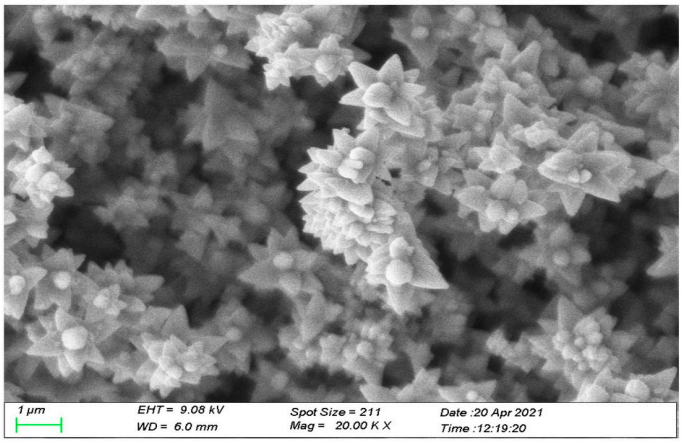

Figure 2. SEM of as synthesized ZnO nanoparticles from 30 mM $ZnNO_3$ solution.

3.2. pH Profile Studies

Figure 3 shows the adsorption of As(III) and As(V) over the pH range from 2 to 6 at room temperature. The binding of the As(III) and As(V) was almost pH-independent across the studied range. A slight decrease in the binding can be observed in Figure 3 with As(III) and As(V) binding at pH 5. However, even though the As(III) binding does increase again at pH 6, it was still lower than pH 4. Similarly, the binding of the As(V) was lower at pH 6 than at pH 4. Thus, pH 4 was chosen as the optimal binding pH for further reactions. The binding of both As(III) and As(V) has been shown to be pH-dependent when binding to different materials [45–48]. For example, the binding of As(III) to TiO_2 nanoparticles has shown pH independence from pH 2 through pH 5, and has been observed to increase after pH 5 then decrease from pH 6 to 10, whereas the binding of As(V) to TiO_2 nanoparticle has been shown to increase almost linearly from pH 3 through 6.5 and subsequently decrease from pH 6.5 to pH 10 [45]. Jezequel et al. investigated the binding of Arsenate from aqueous solution using TiO_2 nanoparticles, which showed the highest binding was observed at a pH of 2 and a linear decrease in binding was observed up to pH 8 where no binding was observed [46], whereas Feng et al. investigated the binding of As(III) and As(V) to high surface area Fe_3O_4 nanoparticles and showed both ions had high binding at pH 2 [47]. However, the binding decreased with increasing the removal of As(III) using ZnO nanoparticles. After calcining the particles at 500 °C for 3 h in a limited air supply, the pH study showed a decrease in binding with increasing pH from 2 to 10 [48]. The pH results in the current study are consistent with those reported in the literature for arsenic binding to other materials [30,49–56]. In addition, pH independence of the binding of As has been observed with the binding of As(III) and As(V) by Fe_7S_8 nanoparticles, $MnFe_2O_4$ and Mn_3O_4, in the pH range of 2–6 [30,40], whereas Fe_2O_3 and Fe_3O_4 have shown pH-independent binding at higher pHs 6 through 10 [41]. The pH-independent behavior of the binding has been shown to be related to the surface charge of the nanoparticles and the arsenic species in solution. In the literature, the point of zero charge for ZnO has been determined to be at pH 9.4, and the isoelectric point has been determined to be at pH 6.4 [57]. Below the PZC pH 9.2, the nanomaterials have a positive charge, while above the PZC, the surface of the nanomaterial will become negatively charged. Thus at a pH below the PZC, the nanoparticles will have a positive charge and attract the arsenic ions. Above the PZE, the nanoparticles will repulse the As ions. Alternatively, the pH-independent binding behavior may be due to the relatively low concentration of As and the high number of active sites on the nanomaterial surface. A high number of surface binding sites and a low concentration of ions in solution would ensure the complete binding of the As(III) and As(V) to the nanomaterial surface and would not show a strong dependence on pH. Furthermore, the lack of surfactant used in the synthesis of the nanoparticles may have generated nanoparticles with a highly active clean surface for As binding. In the present study, a nanomaterial that showed low pH dependency has been synthesized

without the requirement of surfactants or calcination at high temperature. The lack of calcination and surfactant results in the generation of a more cost-effective adsorbent for the removal of As(III) and As(V) from aqueous solution. In addition, the low dependence on pH makes the nanomaterial possibly effective in the treatment of industrial waste as well as drinking water.

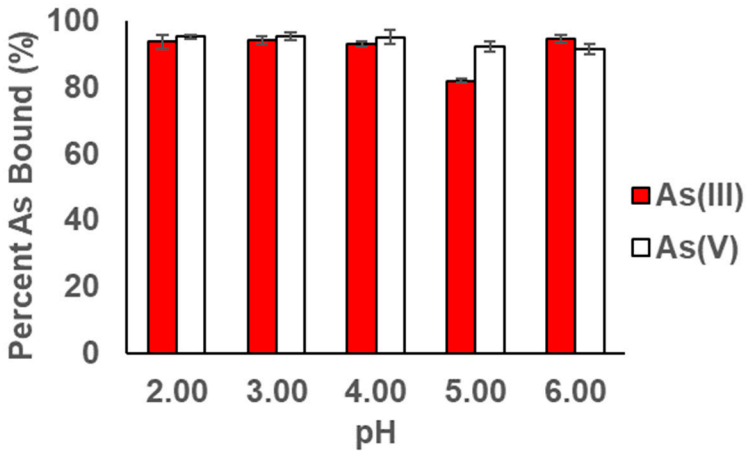

Figure 3. Effect of pH on the binding of both As(III) and As(V) to the synthesized ZnO nanomaterials.

3.3. Zeta Potential of the ZnO Nanoparticles

Figure 4 shows the Zeta potential of the synthesized non-surface functionalized ZnO nanoparticles measured in aqueous solution at pH 2 through 6. As can be seen in Figure 4, the Zeta potential is very and slightly positive and close to neutral from pH 2 through pH 4. At pH 5, the zeta potential starts to become negative, and the negative value increases to a larger value at pH 6. The low zeta potential indicates the suspension with a low stability and high aggregation, which is supported by the presence of clustered nanoparticles observed in the SEM images shown in Figure 2 [58]. The Zeta potential also indicates a small positive or neutral surface charge present on the nanoparticles up to pH 5 where the surface charge becomes negative [59]. Uncoated ZnO nanoparticles showed positive surface charges [59]. The surface charge is reflected in the pH adsorption data for the As(III) and As(V) adsorption studies, as shown in Figure 3.

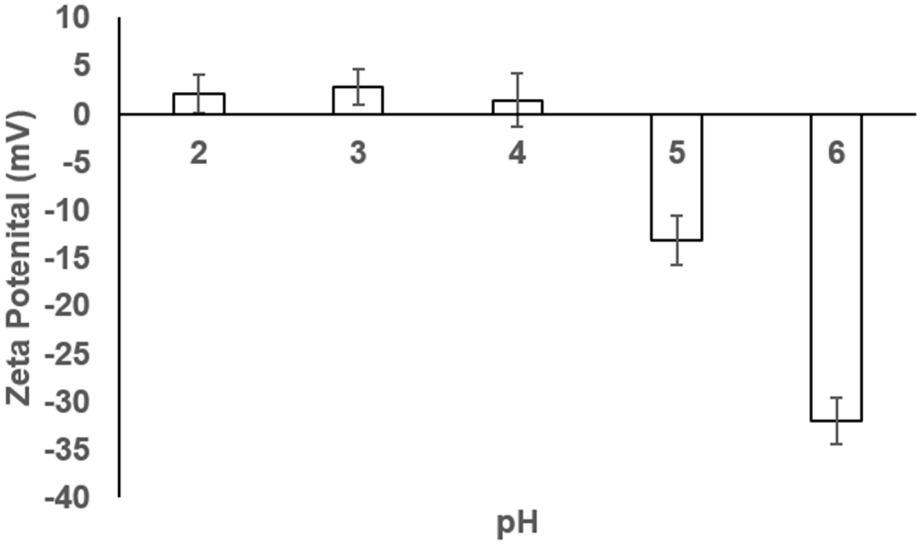

Figure 4. Zeta potential of synthesized ZnO nanoparticles measured at pH 2 through pH 6.

3.4. Particle Characterization after Reaction

The XRD patterns of the ZnO after reacting with either As(III) or As(V) are presented in Figure 5A,B, respectively. The patterns of the reacted ZnO show the same diffraction peaks the 100, 002, 101, 102 and 110 at the same position as the unreacted ZnO, indicating that the As does not influence the crystalline structure after reaction. Furthermore, using Scherrer's analysis of the diffraction peaks, the average grain size of the ZnO after reaction with As(III) was 61.96 nm ± 0.97 and with As(V) was 71.56 nm ± 1.58, whereas the unreacted ZnO nanoparticles had an average size of 62.03 ± 4.06 nm. The data indicate no significant change in the ZnO nanoparticle size before and after reaction with As, which indicates the ZnO nanoparticles are stable. Furthermore, the Le Bail fitting of the ZnO after reaction with either As(III) or As(V), which is presented in Table 3, shows no change in the lattice parameters of the ZnO after reaction. The X^2 values for the fittings indicate a great agreement between the current experimental data and those reported in the literature on the same material. Also, there were no new phases observed in the diffraction patterns.

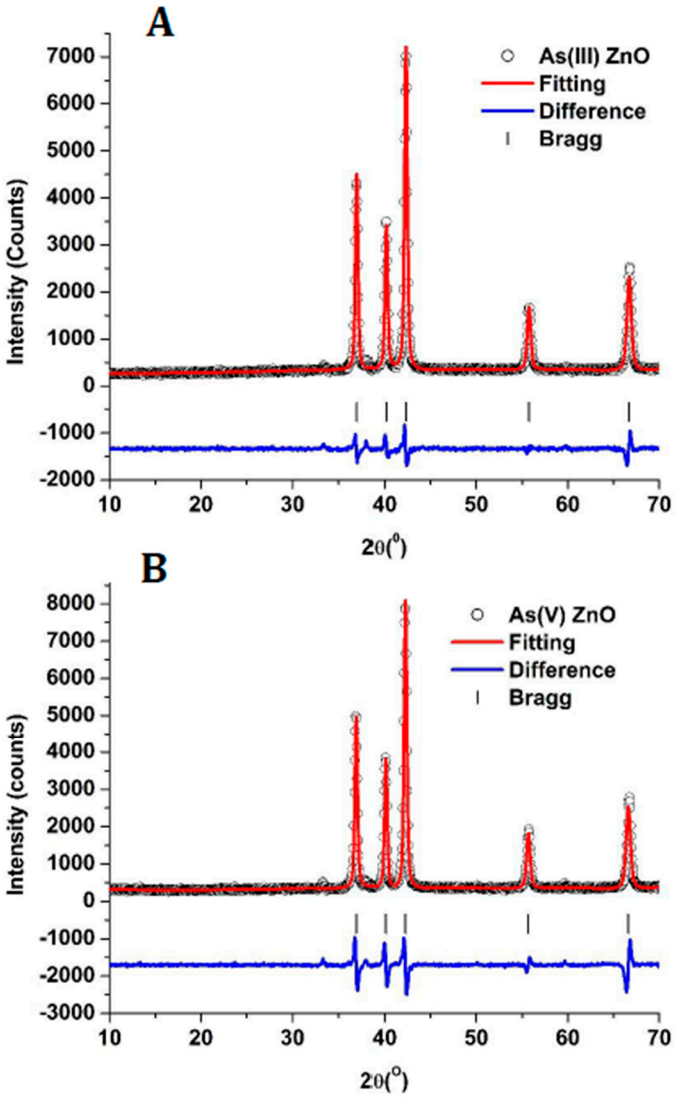

Figure 5. Powder X-ray diffraction patterns of ZnO after reaction with As(III) (**A**) and As(V) (**B**).

Table 3. Le Bail fitting results of ZnO nanoparticles after reaction with As(III) and As(V).

Sample	a (°A)	b (°A)	c (°A)	α°	β°	γ°	χ^2
As(III)ZnO	3.245(8)	3.245(8)	5.214(8)	90.0	90.0	120.0	3.08
As(V)ZnO	3.261(1)	3.261(1)	5.220(9)	90.0	90.0	120.0	3.35

Figure 6 shows the Raman spectra collected for the ZnO nanoparticles before and after reaction with As(III) and As(V). The ZnO stretches are identified in red in Figure 6 and the Identified As-O stretches are shown in black. ZnO vibrations were located at 382 cm^{-1} ($A_{1(LO)}$), 333 cm^{-1} (E_{1high}-E_{1Low}), 438 cm^{-1} (E_{2high}), 546 cm^{-1} ($2B_{low}$), 576 cm^{-1} (A_{1LO}) and 662 cm^{-1} (TA + LO); these are consistent with the peaks identified in the literature. The Raman results are consistent with the ZnO spectra in the literature [60–62].

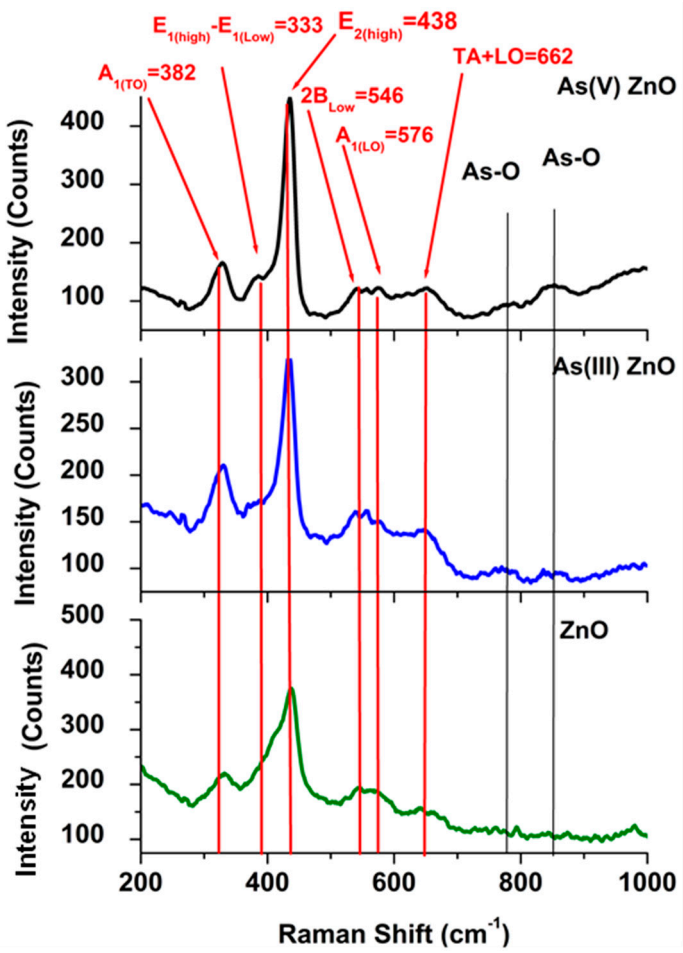

Figure 6. RAMAN spectra of ZnO reacted with As(III), ZnO reacted with As(V), and pure ZnO nanoparticles.

In the As-O region, two broad weak vibrations were observed centered at 770 cm^{-1} and 856 cm^{-1}. In several minerals containing As(V), the As-O interaction is observed in the range 767–778 cm^{-1} [63–66]; the authors assigned these stretches asymmetric stretching of the As-O interaction. The As(V) (As-O symmetric stretch) bound to schwertmannite, an Fe-O-based mineral, which has been observed at 854 cm^{-1} [67,68]. In the present study, the stretches at 770 cm^{-1} and 856 cm^{-1} are consistent with the literature and were assigned to the asymmetric As-O stretching and the symmetric As-O stretch, respectively. The spectra do not show As(III) stretches after binding, signifying that As(III) was oxidized to As(V). The oxidation of the As(III) to As(V) was not completely unexpected as the reactions were

performed in air; the As(III) may have oxidized after binding to the ZnO surface. However, the data confirm that the arsenic was surface-bound to the ZnO.

3.5. Adsorption Isotherms

The adsorption of both As(III) and As(V) ions to the ZnO nanoparticles was observed to follow the Langmuir isotherm. The linear form of the Langmuir isotherm equation is given below:

$$\frac{1}{q_e} = \frac{1}{q_m} + \frac{1}{K_a q_m C_e} \quad (2)$$

where q_e is defined as the removal capacity at any concentration, q_m is the maximum binding capacity, C_e is the equilibrium concentration, and K_a is the Langmuir adsorption constant. Figure 7 shows the Langmuir isotherm plots for the binding of both As(III) and As (V) to the ZnO nanomaterial at 4, 22, and 45 °C. The isotherm plots had correlation coefficients (R^2) of 0.99 or better. Table 4 shows the binding capacity of ZnO nanoparticles for the As(III) and As(V) ions at 4, 22, and 45 °C. Table 4 shows the binding capacity of ZnO nanoparticles for the As(III) and As(V) ions at 4, 22, and 45 °C. Table 4 shows the binding capacity of ZnO nanoparticles for the As(III) and As(V) ions at 4, 22, and 45 °C. As can be seen in Table 4, the highest binding capacities for As(III) and As(V) were 5.8 mg/g and 14.68 mg/g, respectively, and were observed at 4 °C. At the highest tested temperature, 45 °C, the ZnO showed the lowest binding capacities for both As(III) and As(V) than at 4.4 and 12.1 mg/g. The lower binding capacities are more than likely due to the thermodynamics of the reaction, as discussed below, the binding reaction was exothermic. The lower binding of the As(III) is typical for nanomaterials; in general, As(V) is more readily adsorbed than As(III) [36,69,70]. Different studies have shown increased removal of As(III) based on the oxidation of As(III) to As(V) and subsequent adsorption to nanomaterials. Furthermore, it has also been observed that metal oxides generally have a higher capacity to remove As(V) than As(III) [27]. Other metal oxide nanomaterial-based adsorbents have shown high binding capacities for both As(III) and As(V). For example, Mn_3O_4 has shown binding capacities in the range of 10–11.5 mg/g [50]. Parsons et al. showed $MnFe_2O_4$ nanomaterials had binding capacities of 0.7 and 2.1 mg/g for As(III) and As(V) at pH 4, respectively. [30]. Luther et al. showed that As(III) to Fe_2O_3, and Fe_3O_4 had binding capacities of 1.3 and 8.5 mg/g within 1 h of contact at pH above 7. Luther et al. further showed As(V) had binding capacities of 4.6 and 6.7 mg/g to Fe_2O_3 and Fe_3O_4 nanomaterials, respectively [41]. TiO_2 has shown binding capacities close to 30 mg/g, which has been shown to be dependent on the TiO_2 phase present [56]. ZnO nanoparticles coated with acetate have shown a binding capacity of 25.9 mg/g [71], while ZnO embedded in aluminosilicate has been shown a binding capacity of 123.94 mg/g [72]. ZnO nanorods have been found to have a binding capacity up to 52.63 mg/g at pH 7 [73]. The variation in binding capacities may be due to the specific isotherm model used to determine the binding capacities. For example, Yuvaraja et al. used a Langmuir isotherm on the ZnO nanorods, and the binding capacity changed dramatically from 52.62 mg/g with the Temkin isotherm model to 0.00165 mg/g or 1.65 µg/g The binding capacity results of the current study fall within the range of binding capacities reported in the literature for metal oxide-based nanomaterials. In fact, the binding capacities for the current study using ZnO nanomaterials are on the higher end for metal oxide nanoparticles and especially for non-surface modified nanoparticles. The high binding capacities indicate the ZnO NPs would result in a material that potentially has long lifetime. A long lifetime, due to the binding capacity in conjunction with the cost-effective synthesis could reduce the cost of water treatment.

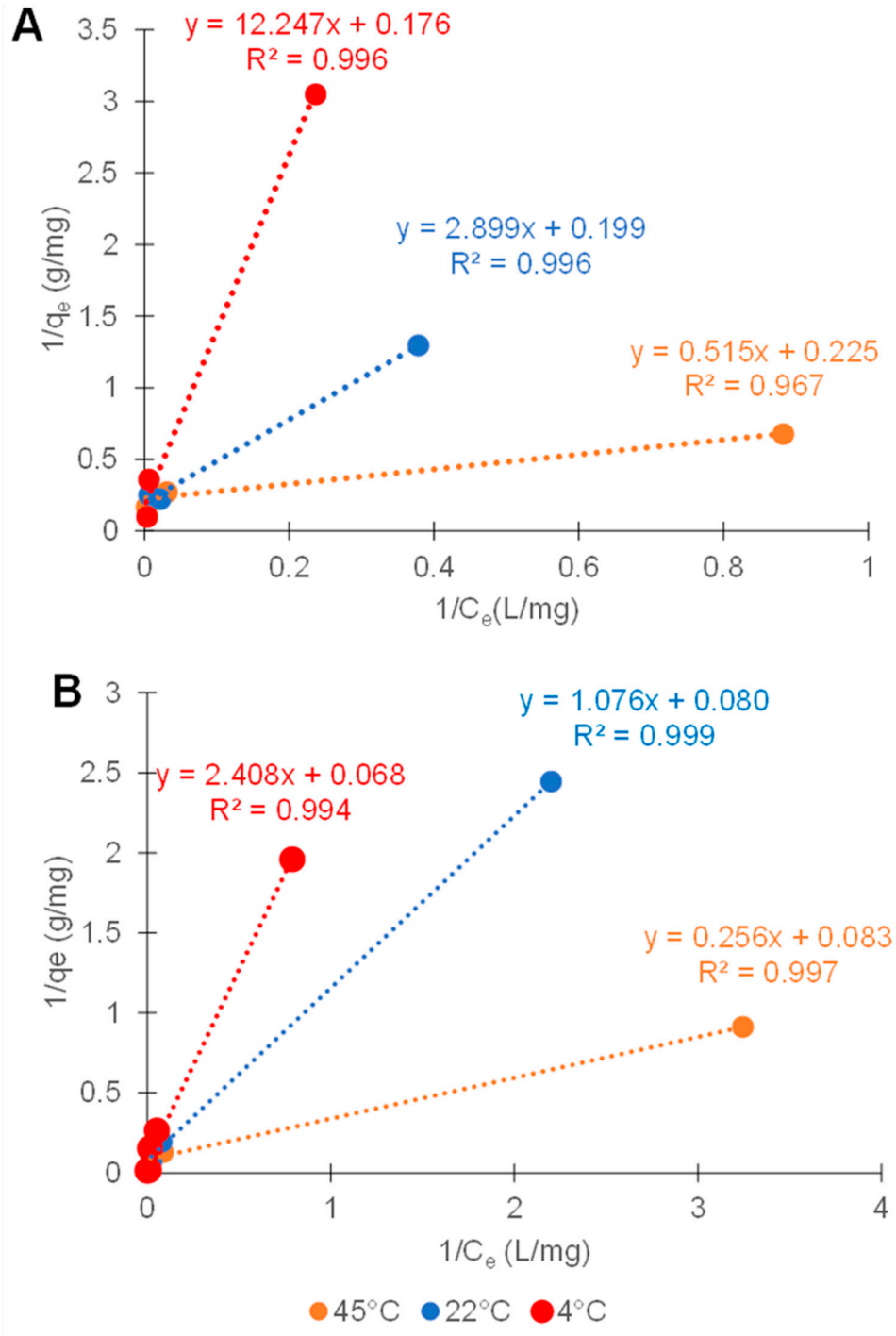

Figure 7. (**A**) Langmuir isotherm plot of the binding of As(III) to the ZnO synthesized nanomaterials. (**B**) Langmuir isotherm plot of the binding of As(V) to the ZnO synthesized nanomaterials.

Table 4. Binding capacity for As(III) and As(V) to the synthesized ZnO nanomaterial.

Sample	Capacity (mg/g)
As(III) 4 °C	5.83
As(III) 22 °C	5.03
As(III) 45 °C	4.44
As(V) 4 °C	14.68
As(V) 22 °C	12.56
As(V) 45 °C	12.09

Table 5 shows the thermodynamic parameters for the adsorption of As(III) and As(V) at 4, 22 and 45 °C. In addition, Figure 8 shows the thermodynamic plots for the binding of both As(III) and As(V) to the ZnO nanomaterials. The Gibbs free energy of the process was determined using the equation below based on the distribution coefficient:

$$\Delta G = -RTlnK_d \quad (3)$$

where ΔG is the change in Gibbs free energy, R is the gas constant (8.314 J mol^{-1} K^{-1}), T is the temperature in Kelvin, and K_d is the distribution coefficients. The Gibbs free energy in an equilibrium process can be related to the equilibrium constant for a reaction or the distribution constant, as shown above. The relationship between ln K_d can be substituted in the Gibbs free energy equation and be related to ΔH and ΔS, as shown in the equation below:

$$lnk_d = \frac{\Delta S}{R} - \frac{\Delta H}{RT} \quad (4)$$

where k_d is the distribution coefficient, ΔS is the change in entropy, ΔH is the change in enthalpy, T is the temperature in Kelvin, and R is the gas constant (8.314 J mol^{-1} K^{-1}). The values of enthalpy and entropy changes were calculated from the slope and the intercept of the plot of $ln\ K_d$ versus $1/T$. Figure 8A shows the thermodynamic plot for the binding of As(III) to the ZnO, and Figure 8B shows the thermodynamic plot for the binding of As(V) to ZnO. The calculated thermodynamic data are shown in Table 5; the enthalpy change for As(III) and As(V) sorption was determined to be −63.44 kJ mol^{-1} and −47.29 kJ/mol kJ mol^{-1}, respectively. From the enthalpy data both the As(III) and As(V) bind to the ZnO through an exothermic reaction, as dictated by the negative sign. The higher observed enthalpy for the binding of As(III) may be due to the oxidation of the As(III) in conjunction with the chemisorption process. The oxidation of the As(III) was indicated in the Raman data, a chemical process may have increased the enthalpy of the reaction. The Gibbs free energy for the sorption process for both As(III) and As(V) was observed to be spontaneous at low and medium temperatures and became nonspontaneous at the highest temperature, 45 °C, as can be seen in Table 5. The increase in ΔG with increasing temperature indicates the binding reaction becomes less favorable for both As(III) and As(V), indicating the binding is occurring through an exothermic reaction. Exothermic binding for As(III) and As(V) has been observed for different materials, including Fe_7S_8, ZnO, CeO_2, CuO nanomaterials, and As(V) binding to red mud [40,51,73–76]. These results suggest that As(III) and As(V) adsorption onto ZnO nanoparticles is an exothermic process and proceeds through chemisorption. As(V) ΔH is around −40 kJ/mol and indicates chemisorption may be the binding mechanism. However, the As(III) enthalpy was very high at −63.4 kJ/mol, which is well above the accepted 40 k/mol, the maximum energy value for physisorption. It has been shown in the literature that chemisorption occurs at enthalpies between 40 and 200 kJ/mol [77–79]. The higher enthalpy for As(III) binding may also be a reflection of the reaction occurring between As(III) and ZnO, causing the oxidation of the As(III), as is indicated by the binding shown in the Raman data. The Raman results for both, the As(III) and As(V) binding to the ZnO after reaction, are shown in Figure 6 and show that only As(V) is present. The absolute values of enthalpy of binding for both As(III) and As(V) are comparable to values reported in the literature on other nanomaterials. For example, Cantu et al. determined that the binding of As(III) and As(V) had binding enthalpies of 43.5 and 7 kJ mol^{-1}, respectively [40]. Goswami et al. showed that As(III)showed an enthalpy of binding of 120 kJ mol^{-1} to copper(II) oxide nanoparticles [51]. Lui et al. showed As(III) and As(V) binding to magnetite particles, which had enthalpies of 13.5 and 13.7 kJ/mol, respectively [69], whereas the Gibbs free energy was in the range of −35 kJ/mol, and the entropy was positive 163 kJ/mol and 154 kJ/mol for the As(V) and As(III), respectively. The binding of As(III) and As(V) to the magnetite nanoparticles was spontaneous at all temperatures and followed an endothermic reaction. From the results of the thermodynamics of the binding process in the present study, As(V) is preferentially bound to the ZnO nanoparticles compared to As(III).

Table 5. Thermodynamic parameters for binding of As(III) and As(V) to synthesized ZnO nanomaterial.

Sample	ΔG (kJmol^{-1})	ΔH (kJ mol^{-1})	ΔS (J mol^{-1}K^{-1})
As(III) 4 °C	−5.76		
As(III) 22 °C	−2.60	−63.4	−233.6
As(III) 45 °C	1.72		
As(V) 4 °C	−2.04		
As(V) 22 °C	−0.18	−47.29	−164.25
As(V) 45 °C	3.52		

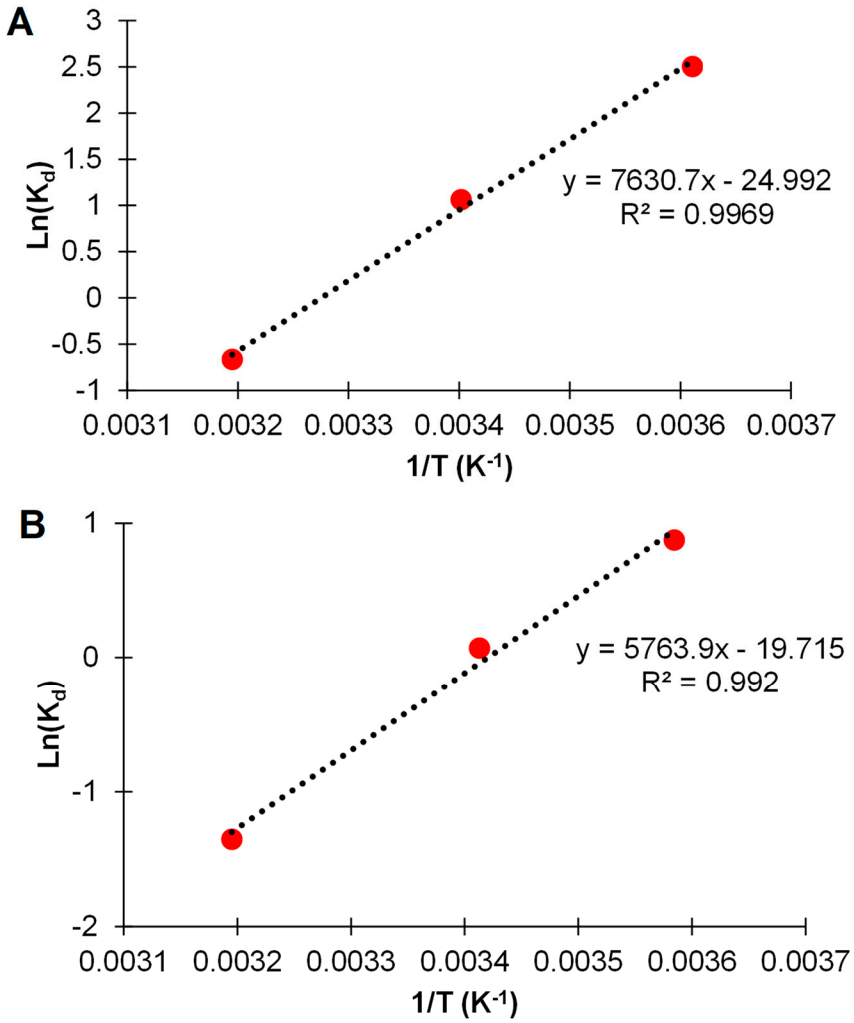

Figure 8. (**A**) Thermodynamics plot for the binding of As(III) to the ZnO synthesized nanomaterials. (**B**) Thermodynamics plot for the binding of As(V) to the ZnO synthesized nanomaterials.

3.6. Time Dependency Studies

Figure 9 shows the results of the time dependency for the binding of As(III) and A(V) to the ZnO nanomaterials at room temperature (22 °C). Both, As(III) and As(V) show increasing binding with increasing time. The As(III) binding at room temperature shows increasing binding of the As(III) up to 1 h of contact time, and the binding becomes constant thereafter. Similarly, the As(V) binding to the synthesized ZnO nanomaterial showed increasing binding up to approximately 60 min and was constant between 60 and 90 min. For both ions, the majority of the binding occurs in the first 15 min of contact and increases gradually with increasing contact up to 60 min and becomes relatively constant thereafter. This behavior has been observed in the literature, with the saturation of the binding sites occurring very quickly. Cantu et al. observed similar behavior for As(III) and

As(V) binding to F_7S_8 [40]. The majority of the binding was observed to occur in the first 15 min of contact, which is fast compared to many of the adsorbents where the authors reported adsorption over more than 24 h of contact time. The binding was fast and high in comparison to other nanomaterials studied in the literature.

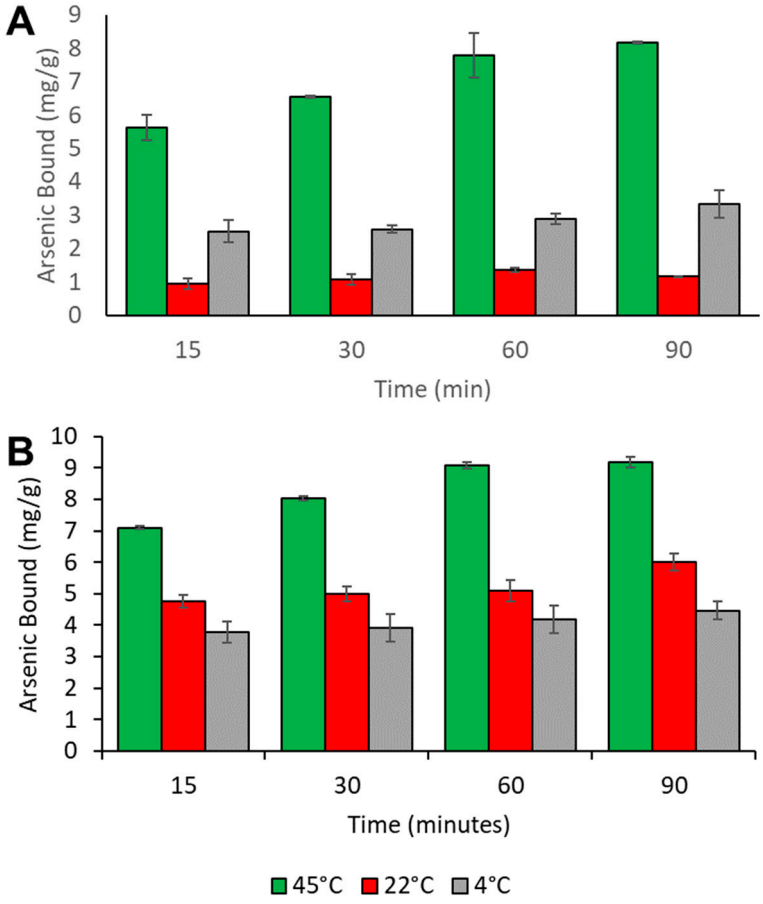

Figure 9. (**A**) Time dependency for the binding of As(III) to the ZnO synthesized nanomaterials. (**B**) Time dependency for the binding of As(V) to the ZnO synthesized nanomaterials.

4. Conclusions

The present study investigated the use of ZnO nanoparticles as an adsorbent for the treatment of water contaminated with As(III) and As(V). The binding indicated no pH dependence from 2 to 4 and a slight decrease in the binding at pH 5 and pH 6. The adsorption experimental results indicated that arsenic removal was best accomplished for As(V). Batch adsorption studies performed showed that the adsorption of As(III) and As(V) was rapid. The maximum adsorption of both As(III) and As(V) was observed at pH 4.0 with percent As removals of 93% and 95% for As(III) and As(V), respectively. The isotherm studies were determined to fit the Langmuir isotherm model, indicating a monolayer adsorption of the ions. The data obtained from adsorption isotherms at different temperatures were used to calculate the thermodynamic parameters ΔG, ΔH, and ΔS of adsorption. The enthalpy for the adsorption was observed for both As(III) and As(V) was negative and indicated an exothermic adsorption process. The values of ΔG for As(III) and As(V) binding were found to be negative at the low and intermediate temperatures, indicating spontaneous binding. However, positive ΔG were observed at the highest temperatures, indicating the reaction became nonspontaneous at higher temperatures. Furthermore, the ΔG data confirmed the adsorption was exothermic. The thermodynamic data indicated that the reaction occurred through chemisorption for both As(V) and As(III) ions, based on the ΔH values of -47.29 and -63.4 kJ/mol, respectively. Chemisorption is

usually characterized by a formation of a bond between the nanomaterial and adsorbate indicating a very strong bond. The formation of a strong bond would reduce the ability of As release during its binding back into the solution. In addition, the binding was shown to occur within the first 60 min and remain constant thereafter.

Author Contributions: Conceptualization, J.G.P.; Investigation, H.M.M., G.T. and T.M.E.; Writing–original draft, H.M.M.; Writing–review & editing, A.M., M.A., E.P. and J.G.P.; Funding acquisition, M.A. and J.G.P. All authors have read and agreed to the published version of the manuscript.

Funding: This research was funded by the UTRGV Chemistry Departmental Welch Foundation Grant (Grant No. BX-0048), and the NSF PREM (DMR-2122178).

Institutional Review Board Statement: Not applicable.

Informed Consent Statement: Not applicable.

Data Availability Statement: The data presented in this study are available through request to the corresponding author.

Acknowledgments: J.G. Parsons acknowledges and is grateful for the support provided by funding from the UTRGV Chemistry Departmental Welch Foundation Grant (Grant No. BX-0048), and M. Alcoutlabi acknowledges funding from the NSF PREM (DMR-2122178) Partnership for Fostering Innovation by Bridging Excellence in Research and Student Success.

Conflicts of Interest: The authors declare no conflict of interest.

References

1. Bissen, M.; Frimmel, F.H. Arsenic—A review. Part I: Occurrence, toxicity, speciation, mobility. *Acta Hydrochim. Hydrobiol.* **2003**, *31*, 9–18. [CrossRef]
2. Choong, T.S.; Chuah, T.G.; Robiah, Y.; Gregory Koay, F.L.; Azni, I. Arsenic toxicity, health hazards and removal techniques from water: An overview. *Desalination* **2007**, *217*, 139–166. [CrossRef]
3. Gorby, M. Arsenic Poisoning. *West. J. Med.* **1988**, *149*, 308–315. [PubMed]
4. Siddique, T.A.; Dutta, N.K.; Choudhury, N.R. Nanofiltration for arsenic removal: Challenges, recent developments, and perspectives. *Nanomaterials* **2020**, *10*, 1323. [CrossRef] [PubMed]
5. Raju, N.J. Arsenic in the geo-environment: A review of sources, geochemical processes, toxicity and removal technologies. *Environ. Res.* **2022**, *203*, 111782. [CrossRef] [PubMed]
6. Tchounwou, P.B.; Udensi, U.K.; Isokpehi, R.D.; Yedjou, C.G.; Kumar, S. 23—Arsenic and cancer. In *Handbook of Arsenic Toxicology*, 2nd ed.; Flora, S.J.S., Ed.; Academic Press: Oxford, UK, 2023; pp. 607–630.
7. Amen, R.; Bashir, H.; Bibi, I.; Shaheen, S.M.; Niazi, N.K.; Shahid, M.; Hussain, M.M.; Antoniadis, V.; Shakoor, M.B.; Al-Solaimani, S.G.; et al. A critical review on arsenic removal from water using biochar-based sorbents: The significance of modification and redox reactions. *Chem. Eng. J.* **2020**, *396*, 125195. [CrossRef]
8. Sharma, V.K.; Sohn, M. Aquatic arsenic: Toxicity, speciation, transformations, and remediation. *Environ. Int.* **2009**, *35*, 743–759. [CrossRef]
9. Jain, C.K.; Ali, I. Arsenic: Occurrence, toxicity and speciation techniques. *Water Res.* **2000**, *34*, 4304–4312. [CrossRef]
10. Pontius, F.W.; Brown, K.G.; Chen, C.J. Health implications of arsenic in drinking water. *J. Am. Water Work. Assn.* **1994**, *86*, 52–63. [CrossRef]
11. Machado-Neves, M.; Souza, A.C.F. *17—The Effect of Arsenical Compounds on Mitochondrial Metabolism*; de Oliveira, M.R., Ed.; Mitochondrial Intoxication; Academic Press: Oxford, UK, 2023; pp. 379–407.
12. Wen, Z.; Li, S.; Zhang, G.; Chen, R.; Zhang, Y.; Liao, X.; Cheng, G.; Chen, R. Effective roxarsone (ROX) and arsenate (As(V)) sequestration from water with magnetic hollow Fe_3O_4-based Mg/Al layered double hydroxide: Performance and mechanism. *J. Clean. Prod.* **2023**, *389*, 136085. [CrossRef]
13. Zhao, F.; Liu, Y.; Zhang, F.; Dong, R.; Yu, W.; Zhang, H.; Han, X.; Gong, P.; Zhang, X.; Liu, Y.; et al. Simultaneous determination and distribution analysis of eleven arsenic species in vegetables. *Microchem. J.* **2023**, *193*, 109168. [CrossRef]
14. Chen, Q.Y.; Costa, M. Arsenic: A Global Environmental Challenge. *Annu. Rev. Pharmacol. Toxicol.* **2021**, *61*, 47–63. [CrossRef] [PubMed]
15. Lee, M.B.; Athar, M. 11—Advances in cutaneous toxicology of arsenic. In *Handbook of Arsenic Toxicology*, 2nd ed.; Flora, S.J.S., Ed.; Academic Press: Oxford, UK, 2023; pp. 327–354.
16. Dos Santos, L.M.G.; Barata-Silva, C.; Neto, S.A.V.; Magalhaes, C.D.; Moreira, J.C.; Jacob, S.C. Analysis and risk assessment of arsenic in rice from different regions of Brazil. *J. Food Compos. Anal.* **2021**, *99*, 103853. [CrossRef]
17. Figoli, A.; Fuoco, I.; Apollaro, C.; Chabane, M.; Mancuso, R.; Gabriele, B.; De Rosa, R.; Vespasiano, G.; Barca, D.; Criscuoli, A. Arsenic-contaminated groundwaters remediation by nanofiltration. *Sep. Purif. Technol.* **2020**, *238*, 116461. [CrossRef]

18. Khan, N.U.; Shahid, M.; Khalid, S.; Natasha, N.; Alothman, Z.A.; Al-Kahtani, A.A.; Imran, M.; Murtaza, B. Arsenic level in groundwater and biological samples in Khanewal, Pakistan. *Environ. Geochem. Health* **2023**. *epub ahead of print*. [CrossRef] [PubMed]
19. Teixeira, M.C.; Santos, A.C.; Fernandes, C.S.; Ng, J.C. Arsenic contamination assessment in Brazil–Past, present and future concerns: A historical and critical review. *Sci. Total Environ.* **2020**, *730*, 138217. [CrossRef]
20. Alka, S.; Shahir, S.; Ibrahim, N.; Ndejiko, M.J.; Vo, D.V.N.; Manan, F.A. Arsenic removal technologies and future trends: A mini review. *J. Clean. Prod.* **2021**, *278*, 123805. [CrossRef]
21. Kabir, F.; Chowdhury, S. Arsenic removal methods for drinking water in the developing countries: Technological developments and research needs. *Environ. Sci. Pollut. Res.* **2017**, *24*, 24102–24120. [CrossRef]
22. Kumar, R.; Patel, M.; Singh, P.; Bundschuh, J.; Pittman, C.U.; Trakal, L.; Mohan, D. Emerging technologies for arsenic removal from drinking water in rural and peri-urban areas: Methods, experience from, and options for Latin America. *Sci. Total Environ.* **2019**, *694*, 133427. [CrossRef]
23. Mohanty, D. Conventional as well as Emerging Arsenic Removal Technologies—A Critical Review. *Water Air Soil Pollut.* **2017**, *228*, 381. [CrossRef]
24. Nicomel, N.R.; Leus, K.; Folens, K.; Van Der Voort, P.; Du Laing, G. Technologies for arsenic removal from water: Current status and future perspectives. *Int. J. Environ. Res. Public Health* **2015**, *13*, 62. [CrossRef] [PubMed]
25. Ng, K.S.; Ujang, Z.; Le-Clech, P. Arsenic removal technologies for drinking water treatment. *Rev. Environ. Sci. Biotechnol.* **2004**, *3*, 43–53. [CrossRef]
26. Nidheesh, P.V.; Singh, T.S. Arsenic removal by electrocoagulation process: Recent trends and removal mechanism. *Chemosphere* **2017**, *181*, 418–432. [CrossRef] [PubMed]
27. Siddiqui, S.I.; Chaudhry, S.A. Iron oxide and its modified forms as an adsorbent for arsenic removal: A comprehensive recent advancement. *Process Saf. Environ. Prot.* **2017**, *111*, 592–626. [CrossRef]
28. Wang, S.; Lu, Y.; Ouyang, X.-K.; Liang, X.X.; Yu, D.; Yang, L.-Y.; Huang, F. Fabrication of chitosan-based MCS/ZnO@Alg gel microspheres for efficient adsorption of As(v). *Int. J. Biol. Macromol.* **2019**, *139*, 886–895. [CrossRef]
29. Zakhar, R.; Derco, J.; Cacho, F. An overview of main arsenic removal technologies. Acta Chim. *Slovaca* **2018**, *11*, 107–113.
30. Parsons, J.; Lopez, M.; Peralta-Videa, J.; GardeaTorresdey, J. Determination of arsenic(iii) and arsenic(v) binding to microwave assisted hydrothermal synthetically prepared Fe_3O_4, Mn_3O_4, and $MnFe_2O_4$ nanoadsorbents. *Microchem. J.* **2019**, *91*, 100–106. [CrossRef]
31. Babaee, Y.; Mulligan, C.N.; Rahaman, M.S. Removal of arsenic (III) and arsenic (V) from aqueous solutions through adsorption by Fe/Cu nanoparticles. *J. Chem. Technol. Biotechnol.* **2018**, *93*, 63–71. [CrossRef]
32. Asere, T.G.; Stevens, C.V.; Du Laing, G. Use of (modified) natural adsorbents for arsenic remediation: A review. *Sci. Total Environ.* **2019**, *676*, 706–720. [CrossRef]
33. Carneiro, M.A.; Pintor, A.M.A.; Boaventura, R.A.R.; Botelho, C.M.S. Current trends of arsenic adsorption in continuous mode: Literature review and future perspectives. *Sustainability* **2021**, *13*, 1186. [CrossRef]
34. Hao, L.; Wang, N.; Wang, C.; Li, G. Arsenic removal from water and river water by the combined adsorption—UF membrane process. *Chemosphere* **2018**, *202*, 768–776. [CrossRef] [PubMed]
35. Lata, S.; Samadder, S.R. Removal of arsenic from water using nano adsorbents and challenges: A review. *J. Environ. Manag.* **2016**, *166*, 387–406. [CrossRef] [PubMed]
36. Massoudinejad, M.; Keramati, H.; Ghaderpoori, M. Investigation of photo-catalytic removal of arsenic from aqueous solutions using UV/H_2O_2 in the presence of ZnO nanoparticles. *Chem. Eng. Commun.* **2020**, *207*, 1605–1615. [CrossRef]
37. Singh, N.; Singh, S.; Gupta, V.; Yadav, H.K.; Ahuja, T.; Tripathy, S.S. A process for the selective removal of arsenic from contaminated water using acetate functionalized zinc oxide nanomaterials. *Environ. Prog. Sustain. Energy.* **2013**, *32*, 1023–1029. [CrossRef]
38. Kataria, N.; Garg, V.K. Optimization of Pb (II) and Cd (II) adsorption onto ZnO nanoflowers using central composite design: Isotherms and kinetics modelling. *J. Mol. Liq.* **2018**, *271*, 228–239. [CrossRef]
39. Gu, M.; Hao, L.; Wang, Y.; Li, X.; Chen, Y.; Li, W.; Jiang, L. The selective heavy metal ions adsorption of zinc oxide nanoparticles from dental wastewater. *Chem. Phys.* **2020**, *534*, 110750. [CrossRef]
40. Cantu, J.; Gonzalez, L.E.; Goodship, J.; Contreras, M.; Joseph, M.; Garza, C.; Eubanks, T.M.; Parsons, J.G. Removal of arsenic from water using synthetic Fe_7S_8 nanoparticles. *Chem. Eng. J.* **2016**, *290*, 428–437. [CrossRef]
41. Luther, S.; Borgfeld, N.; Kim, J.; Parsons, J.G. Removal of arsenic from aqueous solution: A study of the effects of pH and interfering ions using iron oxide nanomaterials. *Microchem. J.* **2012**, *101*, 30–36. [CrossRef]
42. Albertsson, J.; Abrahams, S.C.; Kvick, A. Atomic displacement, anharmonic thermal vibration, expansivity and pyroelectric coefficient thermal dependences in ZnO. *Acta Crystallogr. Sect. B* **1989**, *45*, 34–40. [CrossRef]
43. Rodriguez-Carvajal, J. Recent advances in magnetic structure determination by neutron powder diffraction. *Physica B* **1993**, *192*, 55–69. [CrossRef]
44. Zhou, J.; Zhao, F.; Wang, Y.; Zhang, Y.; Yang, L. Size-controlled synthesis of ZnO nanoparticles and their photoluminescence properties. *J. Lumin.* **2007**, *122–123*, 195–197. [CrossRef]
45. Jegadeesan, G.; Al-Abed, S.R.; Sundaram, V.; Choi, H.; Scheckel, K.G.; Dionysiou, D.D. Arsenic sorption on TiO2 nanoparticles: Size and crystallinity effects. *Water Res.* **2010**, *44*, 965–973. [CrossRef] [PubMed]

46. Jézéquel, H.; Chu, K.H. Removal of Arsenate from Aqueous Solution by Adsorption onto Titanium Dioxide Nanoparticles. *J. Environ. Sci. Health Part A* **2006**, *41*, 1519–1528. [CrossRef]
47. Feng, L.; Cao, M.; Ma, X.; Zhu, Y.; Hu, C. Superparamagnetic high-surface-area Fe_3O_4 nanoparticles as adsorbents for arsenic removal. *J. Hazard. Mater.* **2012**, *217–218*, 439–446. [CrossRef]
48. Rehman, H.; Ali, Z.; Hussain, M.; Gilani, S.R.; Shahzady, T.G.; Zahra, A.; Hussin, S.; Hussain, H.; Hussain, I.; Farooq, M.U.H. Synthesis and Characterization of ZnO Nanoparticles and their use as an Adsorbent for the Arsenic Removal from Drinking Water. *Dig. J. Nanomater. Biostruct.* **2019**, *14*, 1033–1040.
49. Bulut, G.; Yenial, U.; Emirolu, E.; Sirkeci, A.A. Arsenic removal from aqueous solution using pyrite. *J. Clean. Prod.* **2014**, *84*, 526–532. [CrossRef]
50. Garcia, S.; Sardar, S.; Maldonado, S.; Garcia, V.; Tamez, C.; Parsons, J.G. Study of As(III) and As(V) Oxoanion Adsorption onto Single and Mixed Ferrite and Hausmannite Nanomaterials. *Microchem. J.* **2012**, *117*, 52–60. [CrossRef]
51. Goswami, A.; Raul, P.K.; Purkait, M.K. Arsenic adsorption using copper (II) oxide nanoparticles. *Chem. Eng. Res. Des.* **2012**, *90*, 1387–1396. [CrossRef]
52. Guan, X.; Du, J.; Meng, X.; Sun, Y.; Sun, B.; Hu, Q. Application of titanium dioxide in arsenic removal from water: A review. *J. Hazard. Mater.* **2012**, *215–216*, 1–16. [CrossRef]
53. Kong, S.; Wang, Y.; Zhan, H.; Yuan, S.; Yu, M.; Liu, M. Adsorption/Oxidation of arsenic in groundwater by nanoscale FeMn binary oxides loaded on zeolite. *Water Environ. Res.* **2014**, *86*, 147–155. [CrossRef]
54. Lunge, S.; Singh, S.; Sinha, A. Magnetic iron oxide (Fe_3O_4) nanoparticles from tea waste for arsenic removal. *J. Magn. Magn. Mater.* **2014**, *356*, 21–31. [CrossRef]
55. Mamindy-Pajany, Y.; Hurel, C.; Marmier, N.; Romeo, M. Arsenic (V) adsorption from aqueous solution onto goethite, hematite, magnetite and zero-valent iron: Effects of pH, concentration and reversibility. *Desalination* **2011**, *281*, 93–99. [CrossRef]
56. Wen, Z.; Zhang, Y.; Dai, C.; Chen, B.; Guo, S.; Yu, H.; Wu, D. Synthesis of ordered mesoporous iron manganese bimetal oxides for arsenic removal from aqueous solutions. *Microporous Mesoporous Mater.* **2014**, *200*, 235–244. [CrossRef]
57. Fatehah, M.O.; Aziz, H.A.; Stoll, S. Stability of ZnO Nanoparticles in Solution. Influence of pH, Dissolution, Aggregation and Disaggregation Effects. *J. Colloid Sci. Biotechnol.* **2014**, *3*, 75–84. [CrossRef]
58. Chai, M.H.H.; Amir, N.; Yahya, N.; Saaid, I.M. Characterization and Colloidal Stability of Surface Modified Zinc Oxide Nanoparticle. *J. Phys. Conf. Ser.* **2018**, *1123*, 01200.
59. Kim, K.M.; Choi, M.H.; Lee, J.K.; Jeong, J.; Kim, Y.R.; Kim, M.K.; Paek, S.M.; Oh, J.M. Physicochemical properties of surface charge-modified ZnO nanoparticles with different particle sizes. *Int. J. Nanomed.* **2014**, *9* (Suppl. S2), 41–56. [CrossRef]
60. Cusco, R.; Alarcon-Llado, E.; Ibanez, J.; Artus, L.; Jimenez, J.; Wang, B.; Callahan, M.J. Temperature dependence of RAMAN scattering in ZnO. *Phys. Rev. B Condens. Mater.* **2007**, *75*, 165202. [CrossRef]
61. Jaramillo, A.; Baez-Cruz, R.; Montoya, L.F.; Medinam, C.; Pérez-Tijerina, E.; Salazar, F.; Rojas, D.; Melendrez, M. Estimation of the surface interaction mechanism of zno nanoparticles modified with organosilane groups by raman spectroscopy. *Ceram. Int.* **2017**, *43*, 11838–11847. [CrossRef]
62. Song, Y.; Zhang, S.; Zhang, C.; Yang, Y.; Lv, K. Raman spectra and microstructure of zinc oxide irradiated with swift heavy ion. *Crystals* **2019**, *9*, 395. [CrossRef]
63. Frost, R.L.; Martens, W.; Williams, P.A.; Kloprogge, J.T. Raman spectroscopic study of the vivianite arsenate minerals. *Raman Spectrosc.* **2003**, *34*, 751–759. [CrossRef]
64. Frost, R.L.; Čejka, J.; Sejkora, J.; Plášil, J.; Reddy, B.J.; Keeffe, E.C. Raman spectroscopic study of a hydroxy-arsenate mineral containing bismuth–atelestite $Bi_2O(OH)(AsO_4)$. *Spectrochim. Acta Part A Mol. Biomol. Spectrosc.* **2011**, *78*, 494–496. [CrossRef] [PubMed]
65. Liu, C.-H.; Chuang, Y.-H.; Chen, T.-Y.; Tian, Y.; Li, H.; Wang, M.-K.; Zhang, W. Mechanism of Arsenic Adsorption on Magnetite Nanoparticles from Water: Thermodynamic and Spectroscopic Studies. *Environ. Sci. Technol.* **2015**, *49*, 7726–7734. [CrossRef] [PubMed]
66. Mulvihill, M.; Tao, A.; Benjauthrit, K.; Arnold, J.; Yang, P. Surface-Enhanced Raman Spectroscopy for Trace Arsenic Detection in Contaminated Water. *Angew. Chem. Int. Ed. Engl.* **2008**, *7*, 6456–6460. [CrossRef] [PubMed]
67. Burton, E.D.; Bush, R.T.; Johnston, S.G.; Watling, K.M.; Hocking, R.K.; Sullivan, L.A.; Parker, G.K. Sorption of Arsenic(V) and Arsenic(III) to Schwertmannite. *Environ. Sci. Technol.* **2009**, *43*, 9202–9207. [CrossRef]
68. Xu, Z.; Hao, J.; Lib, F.; Meng, X. Surface-enhanced Raman spectroscopy of arsenate and arsenite using Ag nanofilm prepared by modified mirror reaction. *J. Colloid Interface Sci.* **2010**, *347*, 90–95. [CrossRef]
69. Huang, M.; Feng, W.; Xu, W.; Liu, P. An in situ gold-decorated 3D branched ZnO nanocomposite and its enhanced absorption and photo-oxidation performance for removing arsenic from water. *RSC Adv.* **2016**, *6*, 112877–112884. [CrossRef]
70. Vaiano, V.; Iervolino, G.; Rizzo, L. Cu-doped ZnO as efficient photocatalyst for the oxidation of arsenite to arsenate under visible light. *Appl. Catal. B Environ.* **2018**, *238*, 471–479. [CrossRef]
71. Cruz, G.J.; Mondal, D.; Rimaycuna, J.; Soukup, K.; Gomez, M.M.; Solis, J.L.; Lang, J. Agrowaste derived biochars impregnated with ZnO for removal of arsenic and lead in water. *J. Environ. Chem. Eng.* **2020**, *8*, 103800. [CrossRef]
72. Mahato, B.N.; Krithiga, T.; Mary Thangam, M.A. Rapid adsorption of As(V) from aqueous solution by ZnO embedded in mesoporous aluminosilicate nanocomposite adsorbent: Parameter optimization, kinetic, and isotherms studies. *Surf. Interfaces* **2021**, *23*, 100636. [CrossRef]

73. Yuvaraja, G.; Prasad, C.; Vijaya, Y.; Subbaiah, M.V. Application of ZnO nanorods as an adsorbent material for the removal of As(III) from aqueous solution: Kinetics, isotherms and thermodynamic studies. *Int. J. Ind. Chem.* **2018**, *9*, 17–25. [CrossRef]
74. Altundogan, H.S.; Altundogan, S.; Tumen, F.; Bildik, M. Arsenic adsorption from aqueous solutions by activated red mud. *Waste Manag.* **2002**, *22*, 357–363. [CrossRef] [PubMed]
75. Feng, Q.; Zhang, Z.; Ma, Y.; He, X.; Zhao, Y.; Chai, Z. Adsorption and desorption characteristics of arsenic onto ceria nanoparticles. *Nanoscale Res. Lett.* **2012**, *7*, 84. [CrossRef] [PubMed]
76. Yang, W.; Li, Q.; Gao, S.; Shang, J.K. High efficient As(III) removal by self-assembled zinc oxide micro-tubes synthesized by a simple precipitation process. *J. Mater. Sci.* **2011**, *46*, 5851–5858. [CrossRef]
77. Yazdani, M.; Tuutijärvi, T.; Bhatnagar, A.; Vahala, R. Adsorptive removal of arsenic(V) from aqueous phase by feldspars: Kinetics, mechanism, and thermodynamic aspects of adsorption. *J. Mol. Liq.* **2016**, *214*, 149–156. [CrossRef]
78. Navarathna, C.M.; Karunanayake, A.G.; Gunatilake, S.R.; Pittman, C.U.; Perez, F.; Mohan, D.; Mlsna, T. Removal of Arsenic(III) from water using magnetite precipitated onto Douglas fir biochar. *J. Environ. Manag.* **2019**, *250*, 109429. [CrossRef] [PubMed]
79. Monarrez-Cordero, B.E.; Saenz-Trevizo, A.; Bautista-Carrillo, L.M.; Silva-Vidaurri, L.G.; Miki-Yoshida, M.; Amezaga-Madrid, P. Simultaneous and fast removal of As^{3+}, As^{5+}, Cd^{2+}, Cu^{2+}, Pb^{2+} and F^{-} from water with composite Fe-Ti oxides nanoparticles. *J. Alloys Compd.* **2018**, *757*, 150–160. [CrossRef]